

Dynamic surface force measurement. I. van der Waals collisions

Phil Attard^{a)}

Ian Wark Research Institute, University of South Australia, The Levels, SA 5095, Australia

Jamie C. Schulz and Mark W. Rutland

School of Chemistry F11, University of Sydney, NSW, 2006, Australia

(Received 7 July 1998; accepted for publication 12 August 1998)

Theoretical calculations and experimental measurements are used to show that hitherto neglected inertial effects can be significant in computer-controlled surface force measurement devices such as the atomic force microscope. The problem is analyzed in detail for the case of the van der Waals attraction in air. It is demonstrated that equating the cantilever deflection to the surface force systematically underestimates the magnitude of the surface force, increasingly so as the speed of approach is increased. It is also shown that the surface separation becomes lost at high accelerations due to a dynamic uncoupling of the cantilever deflection and angle. The effects of elastic deformation of the bodies are taken into account, including the collision-induced elastic vibrations in the solids. Experimental data are obtained for the van der Waals attraction and collision of glass surfaces in air using the measurement and analysis of surface forces device. All of the effects found in the theoretical calculations are identified in the experimental data. © 1998 American Institute of Physics. [S0034-6748(98)03511-4]

I. INTRODUCTION

A new era in direct surface force measurement began with the advent of computerized data acquisition systems. The modern devices use various electronic techniques to control the motion of the surfaces and electronic or digitally analyzed optical methods to sense the deflection of the force-measuring spring. Here we focus on two of these automated devices: the measurement and analysis of surface forces (MASIF)^{1,2} and the atomic force microscope (AFM).^{3,4} (The various techniques for measuring surface forces have been reviewed elsewhere⁵.) What is different about these new devices compared to the original surface forces apparatus (SFA),⁶⁻⁸ where the interferometric fringes for the separation and forces are measured by eye and recorded manually, is the speed at which the measurements can be performed. Typically the original SFA would take up to several hours to measure a force curve consisting on the order of a 100 data points. The MASIF measures up to 2^{14} data points over as small a time as 0.1 s, and the AFM can record on the order of 2^{10} data on similar time scales. It is this volume of data, fast turnover, and ease of use that has been responsible for the rapidly increasing use of the new devices.

The method of measuring the surface force has not changed over the years. All devices have in common a force measuring spring or cantilever, the deflection of which is measured electronically, optically, or interferometrically.⁵ The surface force F_s is simply equated to the restoring force on the spring, F_k ,

$$F_s = -F_k. \quad (1)$$

The restoring force is given by Hooke's law, $F_k = -kx$, where k is the spring constant and x the deflection of the

spring. This is of course the method that was used in the original static versions of the SFA. The main point of this paper is that Eq. (1) does not apply to the new dynamic force measurement techniques. We shall show that in typical experimental regimes inertial effects can be significant, and that in general the spring deflection in a dynamic measurement lags that of a static measurement, which causes Eq. (1) to underestimate the actual surface force.

Not that static force measurements have entirely ignored the dynamics, since these are implicit in the so-called jump into contact. This occurs at the separation at which the slope of the attractive surface force equals the spring constant, which is the limit of stable equilibrium. An alternative approach to mapping out the force curve is to vary the rigidity of the spring and to measure the static jump point.⁶⁻⁸ Lodge and Mason⁹ further developed this idea with the so-called dynamic jump method. Here oscillations about a point of stable equilibrium allowed motion past the static jump point, provided that the amplitude was small enough so that the spring restoring force exceeded the attractive surface force even though the derivative of the surface force exceeded the spring constant. The amplitude of the oscillations could be gradually increased up until the so-called unstable equilibrium point, the recording of which allowed the force curve to be obtained over a larger domain than in the static jump method. The dynamic jump method of Lodge and Mason⁹ may be seen as a precursor to certain contemporary force measuring techniques that monitor the change in resonant frequency with separation due to the influence of the surface force, such as the AFM in tapping mode,¹⁰⁻¹² or the dynamic mode of a force-feedback version of the MASIF.¹³ Of further relevance to the present day automated devices is the fact that Lodge and Mason⁹ measured the deflection of the force-measuring spring by a capacitor, displaying the re-

^{a)}Electronic mail: phil.attard@unisa.edu.au

sults on an oscilloscope and thereby actually recording the dynamics of the jump into contact. Although the resolution of the device precluded quantitative results, it may be said that Lodge and Mason were ahead of their time in anticipating the modern dynamic devices and data acquisition systems. These authors speculated that Newton's equations might be used to obtain more quantitative information about the dynamics of the system, which is precisely what we do here.

A second dynamic technique is the so-called drainage method of Chan and Horn,¹⁴ in which one surface is driven toward the other at a constant speed. The surface force is deduced by subtracting the known hydrodynamic repulsion F_d ,

$$F_s = -F_k - F_d. \quad (2)$$

The inertial effect we explore here is distinct from this drainage force since it is caused by the finite acceleration of the surfaces under the influence of the surface force. We shall include this drainage term in our calculations below, although in air its main effect is to dissipate energy at contact.

To explore inertial effects, we set out to measure the van der Waals forces between silica glass surfaces in air, which, being free of the usual complications of a liquid interlayer, is the simplest possible system. Thus the measurements lend themselves to unambiguous interpretation. We found a large adhesion but a diminished van der Waals attraction at finite separations, and concluded that inertial effects were responsible. In this system the force law is known, and the dynamical motion is governed simply by Newton's equation. Below we present the theoretical calculations and our experimental data for the van der Waals force between silica glass surfaces in air. We shall primarily model the MASIF device because its higher sampling rate and other design features show the dynamic phenomena in great detail. In the second article in this series¹⁵ we shall model the AFM and compare the results to our measurements of the van der Waals attraction with that device.

There is a second consequence of dynamic force measurements that we find theoretically and experimentally in this article. When a cantilever spring is deflected, in the equilibrium situation (static or steady state) there is a unique relationship between the location of the tip and the angle of the end of the beam. This is exploited in the AFM where the amount of deflection is found by measuring the angle of the tip with a light lever. We point out here that the angle and the deflection are two independent dynamical variables and, depending upon the motion, one cannot simply use the equilibrium relationship to deduce one from the other. This is particularly evident when the surfaces are in contact, where the angle of the tip can change without any further deflection. Our theoretical calculations reveal the nature of the effect, and we discuss its effect on the MASIF data.

There have been a number of previous theoretical calculations of dynamic effects, mainly in the context of noncontact or tapping mode AFM imaging.^{16–20} These analyses deal with a vibrating simple spring and its change in amplitude due to the proximity of the surfaces. In contrast we are concerned with force measurement, not imaging, and we analyze

the deflection of a realistic cantilever spring on a single approach. Our calculations go beyond the earlier studies in that in addition to the van der Waals attraction we include the moment of inertia of the cantilever, the effects of fluid drainage (as distinct from drag forces^{16–18,20}) and the effects of elastic deformation. (Fontaine *et al.*¹⁹ have included drainage at an elementary level, and Ancykowski *et al.*¹⁸ have also included some of the effects of elastic deformation.)

The paper is set out as follows. In Sec. II A, which immediately follows, we develop the simplest model of the experimental setup that shows the major inertial effect discussed above. We present the results of calculations for parameters typical for the MASIF. In Sec. II B we develop a more sophisticated model that shows the additional dynamical feature found in the experiments, namely the decoupling of the angle and position of the cantilever tip. In Sec. II C we explore the effects of elastic deformation of the bodies, and show that elastic vibrations are induced by the collision. In Sec. III we present dynamic force measurement data obtained with the MASIF for the van der Waals attraction in air. We make a detailed comparison of the features in the experimental data that our dynamic calculations revealed.

II. THEORY

A. Simple spring

As mentioned above, all surface force devices are based on controlling the position or separation of the surfaces, and on measuring the force acting between them by means of the deflection of a spring. Usually one of the surfaces is mounted on a piezo-electric motor and its position is a specified function of time. Here we take the driven surface to be the lower surface and we denote its position by $z = z(t)$. (This is the case in the AFM; in the MASIF the geometry is inverted, but this makes no conceptual difference to what follows.) The upper surface is mounted on a spring. In the next section we will model the spring as a cantilever beam, which is a realistic representation of the situation in the AFM and in the MASIF. But to make our first point about dynamic effects it is clearer to use a less sophisticated model, namely a simple coil spring, as shown in Fig. 1. We denote the deflection of the spring by x ; $x = 0$ corresponds to the equilibrium position in the absence of any force between the surfaces (large separations). (Gravity is constant and can therefore be ignored.) The actual separation between the surfaces is $h = x - z$, which is equivalent to choosing the origin for the coordinate of the lower surface such that if the spring were undeflected then the surfaces would be in ultimate contact when $z = 0$. At equilibrium, a positive deflection corresponds to a repulsive surface force, and a negative deflection results from an attraction.

1. The equations of motion

We shall develop and solve the dynamical equations for this model. There are three forces to be taken into account: the spring restoring force F_k , the hydrodynamic (or aerodynamic) drainage force F_d , and the surface force F_s . Denoting the spring constant by k , the elastic restoring force acting on the upper surface in the positive direction (upwards) is

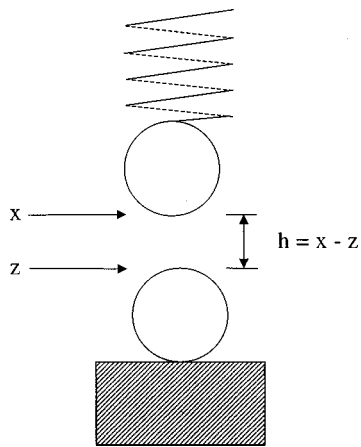


FIG. 1. A simple model of a force measuring device. The lower surface is mounted on a translator and its position is $z(t)$. The upper surface is attached to a simple spring whose extension is $x(t)$, with $x=0$ corresponding to the case of no interaction. The zero for the lower surface is such that the separation is $h=x-z$.

$$F_k = -kx. \quad (3)$$

The drainage force is¹⁴

$$F_d = \frac{6\pi\eta}{h} \left(\frac{R}{2}\right)^2 (\dot{z} - \dot{x}). \quad (4)$$

Here η is the viscosity, which at standard temperature and pressure for air equals $1.8 \times 10^{-5} \text{ kg m}^{-1} \text{ s}^{-1}$, and for water equals $1.0 \times 10^{-3} \text{ kg m}^{-1} \text{ s}^{-1}$. As above h is the separation of the surfaces. The quantity R is the Derjaguin geometrical factor related to the mutual curvature of the two convex bodies; for the two identical spheres depicted in Fig. 1 it equals their radius. The final parenthetical quantity is the mutual speed of approach of the surfaces. The hydrodynamic drainage force is repulsive when the surfaces approach each other, and is attractive when they move apart. The surface force that we shall use in this section and the next is the van der Waals attraction,

$$F_s = \frac{-AR}{12h^2} \left(1 - \frac{z_0^6}{4h^6}\right). \quad (5)$$

Here A is the Hamaker constant, which for glass surfaces in air we take to equal $5 \times 10^{-19} \text{ J}$, and which in water equals 10^{-19} J . (Since the product AR always appears, one could alternatively interpret the present results as applying to bodies with a smaller Hamaker constant and a larger radius of curvature.) This van der Waals force is based upon a Lennard-Jones 6–12 potential. If this is integrated pairwise over the atoms of two semi-infinite planar half spaces and the Derjaguin approximation invoked, then the above 2-8 form for the force results. The second term in parentheses arises from the short-range repulsion between atoms. The quantity z_0 is the separation of lowest energy for two atoms, which here we set equal to 0.35 nm; $h = z_0/2^{1/3}$ is the equilibrium spacing of planar surfaces under zero load. For future use we note that these parameters correspond to a surface energy of $\gamma = A/16\pi z_0^2 = 0.08 \text{ J m}^{-2}$.

We can now use Newton's equation, $F = ma$, to find the motion of the upper surface. Since the position $z(t)$ and ve-

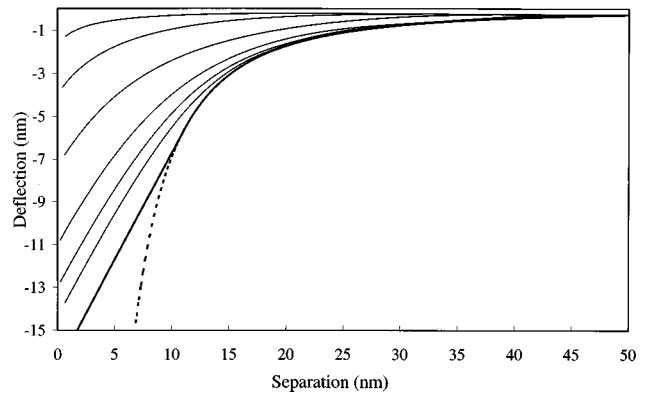


FIG. 2. The deflection due to a van der Waals attraction ($A = 5 \times 10^{-19} \text{ J}$) for the simple spring model. The lowest curve (bold) is the static deflection $x = F_s(h)/k$. After the static jump point, where the tangent equals the spring constant, the continuation of the van der Waals attraction is shown as dotted, since this unstable region is inaccessible. The MASIF, with $R = 1.45 \text{ mm}$, $m = 2.035 \text{ g}$, and $k = 87.2 \text{ N m}^{-1}$. From top to bottom the driving velocity of the lower surface is 6.4, 3.2, 1.6, 0.64, 0.32, and $0.16 \mu\text{m s}^{-1}$.

locity $\dot{z}(t)$ of the lower surface are specified, and since the separation is $h(t) = x(t) - z(t)$, we can take $x(t)$ as the single dynamical variable and regard the forces simply as a function of the deflection and of time, $F = F(x, t)$. With m the mass of the upper surface we have

$$m\ddot{x} = F_k(x) + F_d(x, t) + F_s(x, t). \quad (6)$$

This is a second order nonlinear differential equation for the deflection of the spring. The initial condition is that at $t=0$ the surfaces are far separated, $z(0) \ll 0$, and (generally) that $x(0) = \dot{x}(0) = 0$. In the steady state situation $\ddot{x} = 0$, and Eq. (2) is valid. For stationary surfaces $F_d = 0$ (because $\dot{x} = \dot{z} = 0$) and Newton's equation reduces to Eq. (1). More generally however, one measures F_k while the surfaces are in motion, in which case $\ddot{x} \neq 0$ and Eq. (6) shows that neither Eq. (1) nor Eq. (2) holds.

It proved straightforward to solve this equation numerically to obtain the trajectory of the upper surface. We used simple time stepping, where the new position is $x(t + \Delta_t) = x(t) + \dot{x}(t)\Delta_t$, and the new velocity was $\dot{x}(t + \Delta_t) = \dot{x}(t) + \ddot{x}(t)\Delta_t$. The acceleration is as above, $\ddot{x}(t) = F(x(t), t)/m$. A conservative value of $\Delta_t = 2.5 \text{ ns}$ gave good accuracy; an order of magnitude larger value could be used away from contact and for slower driving speeds.

In the absence of surface and drainage forces (large separations, slow motion), the upper surface executes simple harmonic motion with frequency $f = (\sqrt{k/m})/2\pi$. We tested the computer program by confirming that this frequency appeared in our numerical solutions at large separations for appropriate initial conditions.

2. The effect of inertia

We used the above expressions to model typical measurements of the van der Waals attraction between surfaces in air. The results are shown using representative parameters for the MASIF in Fig. 2. The driving velocities used, $0.1\text{--}10 \mu\text{m s}^{-1}$, span the practical range of the devices. Note that it

is the Hamaker constant times the effective radius of the contact region that enters into the surface force law. The value that we use for this product was determined from the pull-off force (jump-out distance) in the experiments that we report later.

It is clear from the figures that in dynamic force measurement one cannot simply take the measured spring deflection to be equal to the surface force. One can see that the magnitude of the deflection in a static measurement, when $F_k = -F_s$, is larger than that in a dynamic measurement, and that the discrepancy between the two increases with the driving velocity. The effect is due to the inertia of the upper surface, which limits its acceleration in response to the surface force. Before the system has had time to equalize the surface and spring forces, the lower surface has moved further toward the upper one, which decreases the separation and increases the surface force. In consequence the deflection in a dynamic measurement always lags that of a static measurement. The dynamical trajectory of the surfaces must be taken into account for a quantitative measurement of the surface force.

The present calculations follow the motion of the surfaces into contact. There is a relation between the underestimation of the surface force shown in Fig. 2 and the static jump into contact that has previously been used to measure attractive surface forces.⁶⁻⁸ That jump follows the tangent to the van der Waals curve at the point of static equilibrium, and as such also underestimates the actual van der Waals attraction (shown dotted in the inaccessible region). Its relation to the present calculations is that it is the deflection that would occur for an infinitely slow approach of the lower surface. The underestimation that we discuss here is an artifact of dynamic force measurement that arises from the finite speed of the approach of the lower surface.

In these calculations we have included the aerodynamic drainage force, even though in air it has very little effect. It is certainly not the cause of the marked underestimation of the attraction. A close inspection of the trajectory for the fastest speed of approach in Fig. 2 shows an initial *decrease* in the magnitude of the deflection. (The trajectory was started from the equilibrium deflection at 50 nm separation.) This small additional repulsion is typical of the effects of aerodynamic viscosity in these calculations.

There is a certain ambiguity in the choice of spring constant for the MASIF that arises from ignoring the extended tip, and modeling the cantilever beam as a simple spring. The results shown in Fig. 2 are for the force-measuring spring constant, $k = 87.2 \text{ N m}^{-1}$. The sensitivity of the calculations to the spring constant can be gauged from the fact that the measured resonant frequency of 66 Hz, in combination with the measured 2 g mass of the tip would, for a simple coil spring, correspond to a spring constant of 350 N m^{-1} . However using this value instead of $k = 87.2 \text{ N m}^{-1}$ does not qualitatively change the figure. The deflections at contact for the dynamic trajectories decrease by a factor of 1-2, in going from the fastest to the slowest driving speed, and the static van der Waals deflection decreases by about a factor of 4. This observation confirms our expectation that using a stiffer spring will minimize artifacts due to inertia.

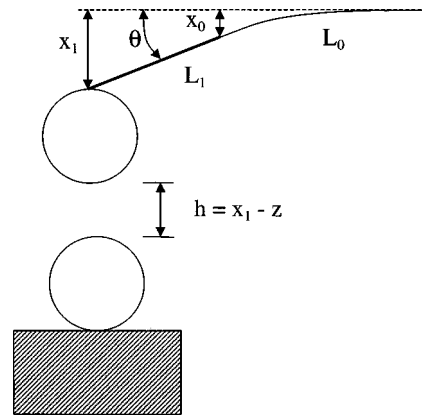


FIG. 3. A more realistic model of the force measuring devices. The lower surface is mounted on a translator and the upper surface is mounted on a cantilever, which consists of a flexible beam of length L_0 , and a rigid tip of length L_1 . The deflection of the end of the beam is x_0 , and the deflection of the end of the tip is x_1 . The tip makes an angle of $\theta = (x_1 - x_0)/L_1$ to the horizontal. (The deflection is greatly exaggerated in the figure; in all cases $x \ll L$, so that $\tan \theta = \theta$.) In the absence of any interaction between the surfaces, $x_1 = x_0 = 0$. The origin of the coordinate system used for the lower surface is such that the separation between the surfaces is $h = x_1 - z$. For the MASIF $L_1 \approx L_0$, and for the AFM $L_1 \ll L_0$.

We deal with the issue of the MASIF spring constant in detail in Sec. II B 2.

In summary, inertial effects can be expected to be significant when the collision time is shorter than the period of the resonant vibrations of the loaded cantilever. To quantify this suppose that the spring deflection can be measured with a resolution Δ_x . Then a change in separation is significant when $\Delta_h = k\Delta_x / |F'(h)|$, which depends upon the gradient of the surface and drainage force. The time for this change in separation to occur is $\Delta_t = \Delta_h / \dot{z}$. Inertial effects will produce measurable artifacts when the characteristic time scale of the cantilever is larger than this. It takes a quarter period for an undeflected cantilever to reach its maximum deflection, where the period of resonant vibrations is $T = 1/f$. Hence in terms of the dimensionless parameter

$$\alpha \equiv \frac{T}{4\Delta_t} = \frac{\dot{z}|F'(h)|}{4fk\Delta_x}, \quad (7)$$

inertia is measurably significant when $\alpha > 1$. In words, inertia is non-negligible for weak springs, fast driving velocities, and at separations where the force is rapidly varying. Inertia is unimportant in systems with high enough resonant frequencies (stiff spring, low mass). Whether or not it is measurable in a given situation depends upon the resolution with which the spring deflection can be measured.

B. Cantilever beam

We now explore a more sophisticated model for the force measuring devices, namely that depicted in Fig. 3. In this model we explicitly take into account the fact that the spring is a cantilever. We shall primarily focus on the MASIF, which has an extended rigid tip with $L_1 \approx L_0$. The model could also be modified and applied to the rectangular beam cantilevers of the AFM. In this case $L_1 \approx L_0/15$ could represent the extra rigidity of the end of the cantilever where

the stylus is attached or alternatively $L_1 \approx L_0/50$ could represent the length of the stylus itself (but at right angles to the cantilever). This and similar models^{21,22} are most appropriate for the analysis of AFM spring constants in static force measurement. Some of the novel features that we find here for the MASIF (such as the distinction between the apparent and the actual position of the surfaces and the influence of torque) will also apply to the AFM in the static case, and we discuss these in detail in the second paper in this series.¹⁵ However since the mass of the AFM cantilever is not negligible compared to the tip, the dynamical problem should really be solved by finite element analysis, which is beyond the scope of the present investigation.

The important dynamical parameters here are the deflection of the end of the flexible cantilever x_0 , the deflection of the end of the rigid tip x_1 , and the tangent at the end of the cantilever θ , which equals the angle of the tip. The deflections that we deal with are exceedingly small: x_0 is typically on the order of nanometers, whereas L_0 is of the order of millimeters. Hence one can always use the small angle approximation, which among other things means that

$$x_1 = x_0 + L_1 \theta. \quad (8)$$

1. Elastic energy

According to the classical theory of elasticity,²³ a force or a torque applied to a cantilever beam causes it to bend, and an amount of elastic energy is stored. In equilibrium the force and torque determine the deflection and angle of the end of the beam, and the elastic energy can be rewritten in terms of these:

$$U_k(x_0, \theta) = \frac{2B}{L_0^3} (3x_0^2 - 3x_0L_0\theta + L_0^2\theta^2). \quad (9)$$

Here $B = EI$ is the elastic parameter that depends upon Young's modulus and the geometric second moment of the beam. Differentiating with respect to the deflection gives the force exerted on the end of the beam,

$$F_0 = \left(\frac{\partial U}{\partial x_0} \right)_{\theta} = \frac{2B}{L_0^3} (6x_0 - 3L_0\theta), \quad (10)$$

and differentiating with respect to angle gives the torque

$$\tau = \left(\frac{\partial U}{\partial \theta} \right)_{x_0} = \frac{2B}{L_0^3} (2L_0^2\theta - 3L_0x_0). \quad (11)$$

These equations may be solved to give the standard expressions for the deflection and the angle in terms of the applied force and torque,²³

$$x_0 = \frac{1}{2B} \left(\frac{2}{3} F_0 L_0^3 + \tau L_0^2 \right), \quad (12)$$

and

$$\theta = \frac{1}{2B} (F_0 L_0^2 + 2L_0 \tau). \quad (13)$$

2. The MASIF spring constant

We now digress to discuss in detail the spring constant of the MASIF in light of these results. Confusion or ambiguity arises in this case because of the extended nature of the rigid tip, $L_1 \approx L_0$, which is not an important consideration in the AFM where $L_1 \ll L_0$. The most important quantity for the measurement of surface forces is the force measuring spring constant, which may also be called the effective spring constant of the device. This may be measured directly by applying a force F_1 at the end of the tip (e.g., by hanging small masses there) and measuring the deflection x_1 at that position. Note that a force F_1 acting on the end of the rigid tip gives a force $F_0 = F_1$ and a torque $\tau = L_1 F_1$ at the end of the flexible cantilever. Using the above relationships and the fact that $x_1 = x_0 + L_1 \theta$ we have for the force measuring spring constant

$$k = \frac{F_1}{x_1} = F_1 \left/ \left[\frac{1}{2B} \left(\frac{2}{3} F_0 L_0^3 + \tau L_0^2 \right) + \frac{L_1}{2B} (F_0 L_0^2 + 2L_0 \tau) \right] \right. \\ = B \left/ \left(L_0^3/3 + L_0^2 L_1 + L_0 L_1^2 \right). \quad (14)$$

The beam flexibility parameter B may be determined from this in terms of the force measuring spring constant and the dimensions of the device, which may be measured.

We confirmed the validity of this model and of the analysis by carrying out a series of measurements for the MASIF. Briefly, we measured $L_0 = L_1 = 15$ mm and $k = 87.2$ N m⁻¹, which gives $B = 6.6 \times 10^{-4}$ J m. For the same cantilever we then placed masses approximately half way along the tip, and measured the deflection of the end of the tip x_1 . In this case the ratio of the force to the deflection was 124 N m⁻¹, which gives, using an appropriately modified form of the above formula, $B = 6.9 \times 10^{-4}$ J m. These values would give an "intrinsic" spring constant for the bare cantilever without its tip of 550–600 N m⁻¹.

We performed further measurements on a similar cantilever, measuring both x_0 and x_1 and obtained values of B in the range $5 - 6 \times 10^{-4}$ J m. These latter measurements were carried out to check whether there was any rotation of the tip about its clamp. We concluded that any such rotation was small enough to be neglected for the present purposes. We actually developed and solved the equations of motion for this more complicated model of the MASIF, and found that the results were essentially the same as the ones given below when no movement of the clamp is allowed.

The difference between the effective spring constant, which is required to measure forces, and the intrinsic spring constant of the bare cantilever, is a consequence of the extended rigid tip and the fact that a cantilever spring is used. The leverage of the tip reduces the stiffness of the system. We emphasize that the piezo-electric bimorphs used in the MASIF do *not* behave as double cantilever springs, and that there is no parallel displacement of the surface upon deflection. We have confirmed this fact by the above measurements, and by analysis of the mechanical and electronic behavior of the device. The importance of the observation is that in calibrating the device the force-measuring spring con-

stant must be obtained in the way described above, and using any other spring constant will lead to systematic errors in the quantitative estimation of the surface forces.

This point can be made in another way by reference to the resonance frequency of the simple model. The mass of the tip is $m=2.035$ g, and using the measured resonance frequency of $f=66$ Hz, one obtains $m(2\pi f)^2=350$ N m⁻¹, which is intermediate between the force measuring spring constant and the bare cantilever spring constant. In other words, one cannot use the resonant frequency and the simple spring model to deduce the effective spring constant of the device. We return to this point below, but in essence the problem is related to the moment of inertia due to the angular motion of the extended tip. It does not arise to the same extent in the AFM, where resonance methods are commonly used to determine the effective spring constant.^{24,25}

3. Equations of motion

We now need to augment the elastic energy with an equation for the kinetic energy. This is just

$$\begin{aligned} T &= \frac{1}{2} \int_0^{L_1} \rho(y) (\dot{x}_0^2 + y \dot{\theta}^2) dy \\ &= \frac{1}{2} \left(m_0 + \frac{m_1}{4} \right) \dot{x}_0^2 + \frac{1}{2} \frac{m_1}{3} \left(L_1 \dot{\theta} + \frac{3}{2} \dot{x}_0 \right)^2. \end{aligned} \quad (15)$$

Here we have modeled the mass density of the beam and tip as consisting of a mass m_0 at the position $y=0$ where the tip is clamped to the beam, and a mass m_1 uniformly distributed along the tip, $\rho(y)=m_0\delta(y)+m_1/L_1$. For the MASIF $m_0 \approx m_1$, and the mass of the beam is negligible. For the AFM the mass of the beam m_b is significant, and the mass of the tip is small, $m_1 \approx m_b L_1/L_0$. The mass m_0 is somewhat less than the mass of the beam, and a reasonable approximation would be to take $m_0=33m_b/140$, which is the effective mass used in resonant frequency calculations for rectangular cantilevers.

The expression for kinetic energy suggests using two generalized coordinates, $q_\alpha=x_0$, with conjugate mass $m_\alpha=m_0+m_1/4$, and $q_\beta=L_1\theta+3x_0/2$, with conjugate mass $m_\beta=m_1/3$. The latter coordinate can also be written $q_\beta=x_1+x_0/2$, and hence the separation is $h=x_1-z(t)=q_\beta-q_\alpha/2-z(t)$. In terms of these the elastic energy becomes

$$\begin{aligned} U_k(q_\alpha, q_\beta) &= \frac{2B}{L_0^3} \left[3q_\alpha^2 - 3q_\alpha \frac{L_0}{L_1} \left(q_\beta - \frac{3q_\alpha}{2} \right) \right. \\ &\quad \left. + \frac{L_0^2}{L_1^2} \left(q_\beta - \frac{3q_\alpha}{2} \right)^2 \right]. \end{aligned} \quad (16)$$

The Hamiltonian is the sum of the kinetic and potential energies, $H=T+U$. Since $\dot{q}_i=\partial H/\partial p_i$, by construction we have $p_i=m_i\dot{q}_i$, $i=\alpha, \beta$. Newton's equations then follow from $m_i\ddot{q}_i=\dot{p}_i=-\partial H/\partial q_i$, where the right side is the generalized force. The cantilever force follows from the derivative of the cantilever potential U_k . For the surface force,

$F_s(h)=-dU_s(h)/dh$, we use the fact that $\partial h/\partial q_\alpha=-1/2$, and that $\partial h/\partial q_\beta=1$, which follow from $h=q_\beta-q_\alpha/2-z(t)$. Hence the equations of motion are

$$\begin{aligned} m_\alpha \ddot{q}_\alpha &= \frac{-2B}{L_0^3} \left[\left(6 + 9 \frac{L_0}{L_1} + \frac{9L_0^2}{2L_1^2} \right) q_\alpha - \left(3 \frac{L_0}{L_1} + 3 \frac{L_0^2}{L_1^2} \right) q_\beta \right] \\ &\quad - \frac{1}{2} (F_s + F_d), \end{aligned} \quad (17)$$

$$m_\beta \ddot{q}_\beta = \frac{-2B}{L_0^3} \left[- \left(3 \frac{L_0}{L_1} + 3 \frac{L_0^2}{L_1^2} \right) q_\alpha + 2 \frac{L_0^2}{L_1^2} q_\beta \right] + (F_s + F_d). \quad (18)$$

Note that these equations treat the hydrodynamic force as if it were derivable from a potential. This system is a set of two coupled second order differential equations. It is straightforward to solve these numerically by simple time stepping, as for the simplified model.

4. Resonant frequency

The set of dynamical equations in the absence of surface or drainage forces may be written in matrix form, and the eigenvalues λ_\pm give the resonant frequencies of the normal modes in the usual fashion, $f_\pm = \sqrt{-\lambda_\pm}/2\pi$. It is straightforward to derive the algebraic expressions for these, but since they in themselves are unilluminating we do not reproduce them here. For the case of the MASIF, with $L_0=L_1=15$ mm, $m_0=m_1=1.0$ g, and $B=7 \times 10^{-4}$ J m, we obtain $f_+=60$ Hz and $f_-=470$ Hz, and $k=89$ N m⁻¹. We checked that our numerical calculations gave the low frequency mode, which independently verifies our analysis and its implementation, and also the accuracy of our numerics.

The fundamental frequency calculated for the model is about 10% lower than the measured resonant frequency, and the force-measuring spring constant is about 2% too high. This represents a guide to the accuracy that can be expected from a comparison of the model calculations with the experimental data. In any case the cantilever model of the apparatus yields values that are obviously more consistent with the measured ones than does the simple spring model.

5. Decoupling of the angle and the deflection

Physically the low frequency mode corresponds to in phase oscillation of the beam and of the tip. That is, when the deflection is positive so is the angle of the tip. The high frequency mode corresponds to out of phase oscillation, with the deflection and the angle being of opposite sign. One can imagine that in the fundamental mode the cantilever beam describes essentially a circular arc, whereas in the higher harmonic it has an s shape.

The fundamental mode in essence represents the static equilibrium relationship between the angle θ and the deflection x_0 (in the case of an applied force and no torque). Even with the addition of a torque, in equilibrium there is a one to one relationship between the two. That is, since in equilibrium the applied force determines uniquely both $x_0=x_0(F_1)$, and $\theta=\theta(F_1)$ [as given above in Eqs. (12) and (13), with $F_0=F_1$ and $\tau=L_1F_1$], then we can equally well

regard $\theta = \theta(x_0)$, or $x_0 = x_0(\theta)$. In fact since both x_0 and θ are linearly proportional to the applied force, then they are linearly proportional to each other. This relationship is exploited in the AFM where the light lever actually measures the change in the angle of the tip of the cantilever. By assuming that this is linearly proportional to a change in the deflection, which it is in a static or steady state situation, one can calibrate the device as usual.

However the above dynamical considerations show that the angle and the deflection need not always be proportional to each other. In the case considered above, namely the higher harmonic resonance, they actually had the opposite sign. We shall shortly use our numerical results to show that the decoupling of the angle and the deflection can occur in other common situations.

One consequence of this decoupling is that one loses the location of the upper, spring-mounted surface, and hence also the separation. For the AFM, which measures the angle of the tip θ , the static equations give for the apparent deflection,

$$\tilde{x}_1(\theta) = 2\theta \frac{L_0^3/3 + L_0^2 L_1 + L_0 L_1^2}{L_0^2 + 2L_0 L_1}. \quad (19)$$

Here we use a tilde to denote the fact that this is an apparent deflection that relies upon the equilibrium relationship between the angle and the deflection, and that it can only be guaranteed to represent the actual deflection of the cantilever tip in the static or steady state situation.

The other possibility is that one measures the deflection of the end of the cantilever x_0 and one uses the equilibrium relationship to deduce its apparent angle $\tilde{\theta}(x_0)$ and hence the apparent deflection of the tip, $\tilde{x}_1(x_0) = x_0 + L_1 \tilde{\theta}(x_0)$. Explicitly,

$$\tilde{x}_1(x_0) = 6x_0 \frac{L_0^3/3 + L_0^2 L_1 + L_0 L_1^2}{2L_0^3 + 3L_0^2 L_1}. \quad (20)$$

We use this second model for the MASIF. In actual fact the charge that develops on the piezo-electric bimorph cantilever used in that device is a functional of the shape of the bent cantilever, and it is a simplification to take the measurement as entirely due to the deflection of its end x_0 . Nevertheless it serves to illustrate the consequences of the decoupling of deflection and angle in dynamic force measurement. In both cases the apparent separation is of course $\tilde{h} = \tilde{x}_1 - z$.

We shall show that the decoupling of the angle and the deflection of the cantilever is most apparent in the post-contact experimental data. It is straightforward to calculate the resonant frequency in this situation. When the surfaces are in contact the deflection is essentially constant, which for the present purposes can be taken as $x_1 = 0$. (The steady driving of the lower surface does not affect the frequency of the vibrations.) Hence one now has only one degree of freedom, since the cantilever deflection and angle must satisfy $0 = x_0 + L_1 \theta$. Eliminating x_0 from the kinetic energy one has

$$T = \frac{1}{2} \left(m_0 + \frac{m_1}{4} \right) L_1^2 \dot{\theta}^2 + \frac{1}{2} \frac{m_1}{3} \left(L_1 \dot{\theta} - \frac{3}{2} L_1 \dot{\theta} \right)^2 \equiv \frac{1}{2} M \dot{\theta}^2, \quad (21)$$

which gives an effective mass of

$$M = (m_0 + m_1/3) L_1^2. \quad (22)$$

The cantilever elastic strain energy becomes

$$U_k = \frac{2B}{L_0^3} (3L_1^2 \theta^2 + 3L_1 L_0 \theta^2 + L_1^2 \theta^2) \equiv \frac{1}{2} K \theta^2, \quad (23)$$

which gives an effective spring constant

$$K = 2 \frac{2B}{L_0^3} (3L_1^2 + 3L_1 L_0 + L_1^2). \quad (24)$$

Hence the frequency of vibrations of the cantilever when the surfaces are in contact is

$$f = \frac{1}{2\pi} \sqrt{\frac{K}{M}}. \quad (25)$$

For the parameters used to model the MASIF, this gives $f = 331$ Hz, in agreement with our numerical calculations (see below).

6. Results

Figure 4 shows the calculated trajectory for the MASIF under the influence of a van der Waals attraction at several driving velocities. Both the actual (full curve) and the apparent (dotted curve) deflection and separation are shown. The apparent trajectory is calculated from the actual deflection of the cantilever beam x_0 and the equilibrium angle $\tilde{\theta}(x_0)$, $\tilde{x}_1(x_0) = x_0 + L_1 \tilde{\theta}(x_0)$. Several pertinent features in the curves are numbered in Fig. 4(a), which we now discuss in detail.

At large separations (1) the apparent trajectory coincides with the actual trajectory, and the negative deflection in this regime indicates an attraction. As for the simple spring, Fig. 2, at this driving velocity the dynamic deflection considerably underestimates that of a static measurement of the van der Waals force. What can also just be made out at large separations at the slowest driving speed, Fig. 4(c), is the low frequency free vibration resonant at 60 Hz. Because the initial conditions had the surfaces in static equilibrium at 50 nm separation, the amplitude of these vibrations in these particular calculations is rather small.

As the upper surface jumps into contact (2), there is an increasing discrepancy between the actual position and the apparent position of the end of the tip. In the inset it can be seen that the surface accelerates into contact. This is shown by the increasing separation between the squares, which represent snapshots equally spaced in time. The apparent deflection is almost constant in this regime for this the fastest driving velocity.

When the surfaces first make contact (3), the apparent deflection and separation (4) show a considerable lag. [The points (3) and (4), indicated by filled symbols, coincide in time.] In fact, there is an apparent *decrease* in the deflection

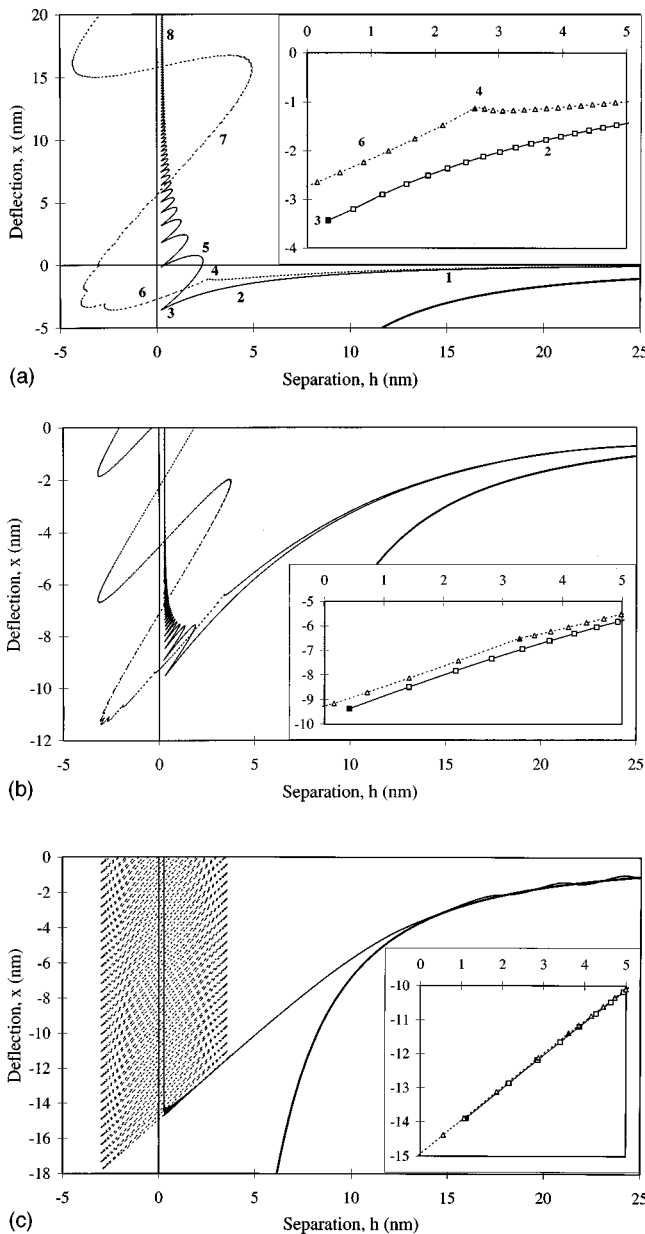


FIG. 4. The deflection at the end of the tip as a function of separation for the cantilever model of the MASIF ($R=1.45$ mm, $m_0=m_1=1.0$ g, $L_0=L_1=15$ mm, and $B=7 \times 10^{-4}$ J m). The bold curve is the static van der Waals attraction ($A=5 \times 10^{-19}$ J, $k=88.9$ N m $^{-1}$), the solid curve is the actual deflection x_1 and separation h , and the dotted curve is the apparent deflection $\tilde{x}_1(x_0)$ and apparent separation $\tilde{h}(x_0)$. The inset shows the jump into contact on an expanded scale; the symbols are equally spaced in time, (different in each figure) with the filled symbols denoting the instant of first contact. (a) The driving velocity is $\dot{z}=6.4 \mu\text{m s}^{-1}$, and the spacing between symbols is 0.025 ms, (b) $1.6 \mu\text{m s}^{-1}$, and 0.075 ms, (c) $0.16 \mu\text{m s}^{-1}$, and 0.1 ms.

and a consequent apparent *decrease* in the mutual speed of approach of the two surfaces up to this point. The difference between the actual and the apparent behavior of the surface is due to the rotation of the extended tip about its center of mass: when the end of the tip accelerates into contact (3), the base of the tip where it is clamped to the cantilever actually moves in the opposite direction (in the frame of reference of the center of mass of the tip) so that x_0 is approximately constant, and hence so is $\tilde{x}_1(x_0)$ (4).

After initial contact the surfaces bounce off each other (5) in consequence of the elastic effects of the collision (see below). The rapid acceleration and change in direction associated with the first bounce is magnified by the apparent motion of the surfaces (6); the reversal in the rotation of the tip about its center of mass causes a rapid change in x_0 and hence in $\tilde{x}_1(x_0)$ and $\tilde{h}(x_0)$. In the absence of the present calculations, which show that the surfaces have actually already come into contact, this apparent acceleration would most likely have been interpreted as *the* jump into contact.

It is the top of the kink, where the jump in the apparent trajectory begins, that signifies the instant of initial contact. This is most evident at high driving velocities. At lower velocities [Figs. 4(b) and 4(c)] apparent contact can be identified by the increase in acceleration of the surface.

The apparent jump into contact (6) is due to a rapid acceleration of the end of the cantilever x_0 , with x_1 essentially fixed at contact (the amplitude of the bounces is about a nanometer). The momentum of x_0 causes it to overshoot its equilibrium position, before decelerating and reversing direction. This simple harmonic motion (7) is the fundamental vibration of the beam in contact. The frequency of these vibrations is the 331 Hz calculated above. The fine structure in the very first period of vibration in Fig. 4(a) reflects the bouncing of the elastic collision.

These post-contact vibrations give an apparent oscillation symmetric about the actual contact position. At low driving frequencies [Figs. 4(b) and 4(c)], the amplitude of the oscillations (half the difference in successive extrema of the apparent separation) is approximately the same as the position of the jump (3.25 and 3.62 nm, respectively, for $\dot{z}=0.16 \mu\text{m s}^{-1}$), whereas at high velocities the amplitude increases and the jump position decreases (4.65 and 2.71 nm, respectively, at $\dot{z}=6.4 \mu\text{m s}^{-1}$).

The amplitude of the vibrations calculated here does not decay because we have not included any dissipative terms in our calculations for the motion of the end of the cantilever x_0 . The amplitude of the actual bounces (8) decays due to the dissipative drainage term acting on \dot{x}_1 . As mentioned above, the bounces arise from the conservation of energy of the elastic collision. The bottom, driving surface acts like an infinitely massive wall. In the moving frame of reference, the top surface would have enough kinetic energy to escape the potential well of the attractive surface force, if that alone were acting. Of course energy is continually being stored, and returned, in the increasing deflection of the spring. Energy is being dissipated by the drainage term that is associated with \dot{x}_1 . The former effect causes an increase in frequency of the bounces, and a small decrease in amplitude. It is the dissipative drainage term that is primarily responsible for the marked decay in the amplitude of the actual bounces (8). This contrasts with the neglect of any dissipative forces for the motion of the cantilever itself \dot{x}_0 . Since the elastic energy due to deflections is additive, the only mechanism in the model for damping the vibrations of the beam is via the motion they induce in \dot{x}_1 , but this is rather weakly coupled. Consequently in this model the amplitude of the apparent oscillations is constant on these time scales. A more realistic

model would include the dissipative terms for the motion of the cantilever itself (e.g., Stokes drag) and for the frictional dissipation due to the consequent shearing and rolling at contact. The latter is the most important, but modeling it is beyond the scope of the present paper.

It should be clear that the apparent oscillatory motion of the surfaces due to the cantilever vibrations is not directly related to the bouncing of the elastic collision of the surfaces. Rather the initial transient of the latter serves to stimulate the resonant frequency of the beam with the end of the tip fixed. The large amplitude oscillations here do not represent the actual motion of the surfaces, but are rather the apparent motion that results from measuring nothing but the vibration of the cantilever. In particular no negative separations can actually occur in this model (infinitely rigid spheres) and after the bouncing has died down the actual separation between the surfaces is approximately the equilibrium separation under zero load, $z_0/2^{1/3} = 0.28$ nm. The surfaces are actually forced closer than this as the load is increased (positive deflections) but only by fractions of a nanometer. In practice modeling the bodies as perfectly rigid spheres is not a good approximation in the post-contact situation, and we now further refine the model to incorporate the effects of elastic deformation of the surfaces on the collision.

C. Elastic deformation

A complete description of dynamic force measurement must include the effects of the elastic deformation of the surfaces due to their mutual interaction. Under a van der Waals attraction, the surfaces themselves (as distinct from the center of mass of the bodies) initially bulge towards each other before jumping into contact due to an elastic instability. As the surfaces are driven further towards each other, flattening occurs under the applied load.

It is most important to account for the effects of mutual elastic deformation of the surfaces just prior to the jump in to contact, and post-contact. We incorporate these effects into the equations of motion using certain analytic approximations for the static force–deformation relation at the continuum level.^{26–28} (Molecular level calculations of elastic deformation under van der Waals interactions have been carried out by Tang *et al.*²⁹) First we need to distinguish between the physical separation of the surfaces of the deformed bodies, which we shall denote by H , and the so-called undeformed separation h . For the perfectly rigid spheres used above the two coincide. For deformable surfaces h is the separation that the surfaces would have in the absence of any interaction; for the two spheres used here it is the distance between their centers minus twice their natural radius. On physical grounds one must always have $H > 0$. (The location of the surfaces is defined by the zero of separation that appears in the surface force law.) On the other hand it is permissible for h to be negative. A negative value indicates that in the absence of any surface force or deformation the surfaces would have interpenetrated. The central deformation is $\delta = H - h$: a negative deformation corresponds to the precontact bulge, and a positive deformation corresponds to flattening under an applied load. The equa-

tions of motion, Eqs. (16) and (17) above, give the undeformed separation $h = x_1 - z(t)$. The precontact surface and drainage force is however now given by $F(H)$, not $F(h)$, and it remains to be shown how to calculate the physical separation H and the deformation δ . Post-contact we use the latter to calculate the force due to elastic deformation.

For the precontact situation we shall use the analytic approximations of Attard and Parker.^{27,28} For the van der Waals attraction, the deformation prior to the jump into contact is given by²⁷

$$\delta = -\sqrt{R} \frac{A}{8} \frac{1 - \nu^2}{E} H^{-5/2}, \quad (26)$$

where E is Young's modulus and ν is Poisson's ratio. (This uses only the attractive H^{-2} part of the van der Waals force since the short-range repulsion is negligible prior to the jump into contact; it would be straightforward to use the whole force law²⁷.) This result gives the deformation as a function of the actual separation H , but the quantity that we actually know at any instant is the undeformed separation $h(t)$ (from the numerical solution of the equations of motion up to this point). However we have another equation that relates the two unknowns, namely $\delta = H - h$. Hence we have two equations in two unknowns, which are easily solved by simple iteration; in practice two iterates sufficed.

Under an attractive surface force there is an elastic instability that causes the surfaces themselves (as distinct from the centers of the two spheres) to jump into contact. This so-called jump separation is given by²⁷

$$H^* = \left(\sqrt{R} \frac{3A}{8} \frac{1 - \nu^2}{E} \right)^{2/7}. \quad (27)$$

Our strategy then is to solve the equations of motion up until the jump separation using the surface and drainage forces calculated at the physical (deformed) surface separation, as just described.

At the jump separation we assume that the physical surfaces instantly jump into contact, $H = H_0 \equiv z_0/2^{1/3}$. The justification for the first assumption is that since it is only a surface jump, the mass associated with it is infinitesimal compared to the mass of the bodies and the tip, and hence it occurs on a much faster scale than any other motion. The justification for the second assumption is that the actual physical separation of the surfaces in contact is always within some tens of picometers of the mutual equilibrium separation of planes, even under much higher loads than are applied here.²⁷

In this post-contact situation we shall use the approximation due to Johnson, Kendall, and Roberts (JKR).²⁶ This gives the elastic deformation δ and the radius of the flattened circular contact region, a_{\pm} , due to an applied load F_{δ} ,

$$a_{\pm}^3 = \frac{3(1 - \nu^2)R}{4E} [F_{\delta} + 3\pi\gamma R/2 \pm \sqrt{3\pi\gamma R F_{\delta} + (3\pi\gamma R/2)^2}], \quad (28)$$

and

$$\delta_{\pm} = \frac{2a_{\pm}^2}{R} - \sqrt{\frac{4\pi\gamma a_{\pm}(1-\nu^2)}{E}}. \quad (29)$$

For the van der Waals attraction used here, the surface energy is $\gamma = A/16\pi z_0^2 > 0$. These two equations give the deformation as a function of the force $\delta(F_{\delta})$ via the intermediary of a_{\pm} , which is discussed below. It is numerically straightforward to invert the relationship to obtain $F_{\delta}(\delta)$. The deformation force represents the force exerted on the upper body by the lower driving body, which causes both to deform by a total amount δ . The deformation must of course be calculated as part of the motion.

The modified forms of the equations of motion Eqs. (17) and (18) are

$$m_{\alpha} \ddot{q}_{\alpha} = \frac{-2B}{L_0^3} \left[\left(6 + 9 \frac{L_0}{L_1} + \frac{9L_0^2}{2L_1^2} \right) q_{\alpha} - \left(3 \frac{L_0}{L_1} + 3 \frac{L_0^2}{L_1^2} \right) q_{\beta} \right] - \frac{1}{2} F(H), \quad (30)$$

$$m_{\beta} \ddot{q}_{\beta} = \frac{-2B}{L_0^3} \left[- \left(3 \frac{L_0}{L_1} + 3 \frac{L_0^2}{L_1^2} \right) q_{\alpha} + 2 \frac{L_0^2}{L_1^2} q_{\beta} \right] + F(H), \quad (31)$$

where

$$F(H) = \begin{cases} F_s(H) + F_d(H, \dot{H}), & H > H^* \\ F_{\delta}(\delta) + F_d(H_0, \dot{z} - \dot{x}_1), & H < H^*. \end{cases} \quad (32)$$

In essence one has three unknowns: h , H , and δ . The equations of motion give the trajectory of $h(t)$. For the current value of $h(t)$, prior to contact one simultaneously solves the two deformation equations, Eq. (26) and $\delta = H - h(t)$. Hence one calculates $h(t + \Delta_t)$ from the equations of motion. In the post-contact situation one has $H = H_0$, and hence for the current $h(t)$ the central deformation is $\delta = H_0 - h(t)$. From the JKR expressions, Eqs. (28) and (29), one calculates $F_{\delta}(\delta)$ and hence $h(t + \Delta_t)$ from the equations of motion.

As mentioned above, prior to contact the deformation equation (26) was solved by simple iteration. Post-contact the JKR expressions, which give $\delta(F_{\delta})$, were solved for $F_{\delta}(\delta)$ by binary search at each time step. In general the positive root for the contact radius is chosen; immediately after the jump into contact it may be necessary to choose the negative root in order to obtain the necessary deformation. More precisely, on the positive branch a_+ , the deformation *decreases* with *decreasing* load for loading forces greater than the so-called controlled force pull-off force, $F_{\delta} = -3\pi\gamma R/4$. If one requires an even smaller, more negative deformation than at this point (a *larger* extension since the surfaces are here under tension) one must go to the negative branch a_- , where the deformation *decreases* under *increasing* load up until the so-called controlled deformation pull-off force, $F_{\delta} = -5\pi\gamma R/12$. Immediately after the jump into contact the extension could possibly be larger than the maximum predicted by the JKR approximation. If this should

occur one would use the controlled deformation pull-off value as the elastic force until the extension decreased sufficiently to use the algorithm just described.

Our treatment of the post-contact situation involves a number of simplifying assumptions. Although these are dynamic calculations, we use the equilibrium relationship between the deformation and the applied forces. This is likely appropriate given that such a small fraction of the total mass is involved in the actual deformation. A related consequence of this assumption is that there is no pinning of the contact line as the two solid surfaces spread on each other, and that the motion of the line is reversible. This assumption is implicit in the JKR theory, in which there is no hysteresis, and is therefore consistent with the present level of analysis. However one should be aware that in practice soft adhesive bodies do show hysteresis in the loading-unloading cycle. Sophisticated numerical calculations show that hysteresis sets in for values of the characteristic elasticity and adhesion parameter $\sigma \equiv \gamma\sqrt{R/2z_0^3}(1-\nu^2)/E$ around unity.²⁷ In the present calculations $\sigma = 5$, and so using the JKR approximation limits the quantitative accuracy of the comparison with experiment in this regime. Finally, and related to the neglect of hysteresis, is the neglect of friction and other dissipative mechanisms in the post-contact mutual wetting of the surfaces. To compensate for this somewhat we have retained the drainage term in the equations of motion, $F_d[H_0, \dot{z} - \dot{x}_1(t)]$, which at some level represents the situation at the circumference of the contact region.

For the parameters used here [$A = 5 \times 10^{-19}$ J, $z_0 = 0.35$ nm, $R = 1.45$ mm, and the elasticity of glass, $E/(1-\nu^2) = 6 \times 10^{10}$ N m⁻²] the equations of Attard and Parker²⁷ give the jump into contact as $H^* = 1.46$ nm and the bulge at the jump as $\delta^* = -0.49$ nm, which give an undeformed surface separation of $h^* = 1.95$ nm. Using the surface energy for the model ($\gamma = 0.08$ J m⁻²), after contact the flattening under zero load amounts to $\delta = 3.3$ nm, according to the JKR result.²⁶ As we shall see the amount of flattening changes little under the loads applied in a typical experiment.

1. Results

In this section, which presents the results of our analysis of the effects of elastic deformation, it is important to distinguish between the *physical* trajectory, which is that of the deformed surfaces themselves, the *actual* trajectory, which is the motion of the undeformed surfaces, and the *apparent* trajectory, which is the motion of the undeformed surfaces deduced from the deflection of the end of the cantilever.

Figure 5 shows the effect of mutual elastic deformation on dynamical force measurements in the MASIF. Essentially four features emerge upon comparison with the respective results in Fig. 4: the more well-defined kink marking the apparent jump into contact at higher driving speeds, the increased amplitude of the vibrations of the cantilever in contact, the negative actual undeformed separation post-contact, and the elastic vibrations in contact.

The kink in the apparent separation that denotes initial contact is much more marked in Fig. 5(a) than in Fig. 4(a). Indeed, the apparent *increase* in separation and *positive* change in the deflection can still be seen at the slower driv-

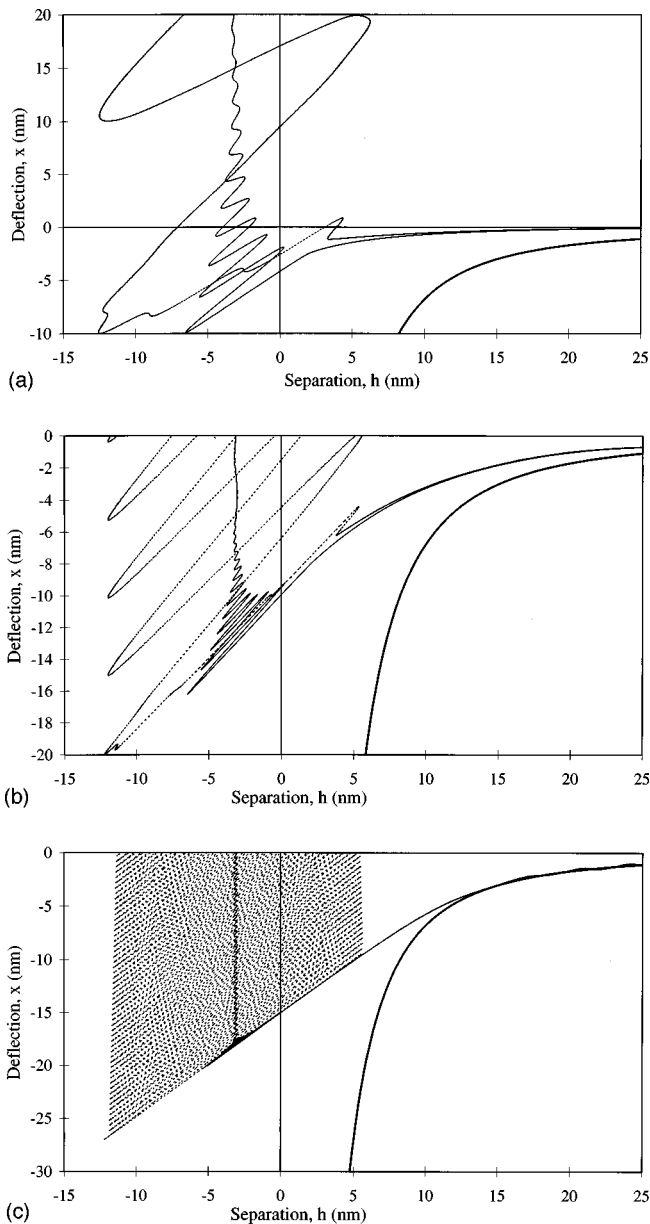


FIG. 5. Tip deflection for the same parameters and respective driving velocities as the preceding figure, but taking into account the elastic deformation of the surfaces [$E/(1-\nu^2)=6\times 10^{10}$ N m $^{-2}$]. The abscissa is the undeformed separation, either actual (full curve) or apparent (dotted curve).

ing speed of $1.6 \mu\text{m s}^{-1}$ [Fig. 5(B)]. Prior to the surface jump separation H^* , the van der Waals attraction is larger than in the undeformed case [$F_s(H^*)/F_s(h^*)=1.8$], but because of the high driving speed the deflection is little affected by this. The real change occurs when the surfaces have jumped into contact and spread on each other. There is an instantaneous increase in the attractive force that is manifest by the change in slope of the actual trajectory at the undeformed separation $h^*=1.95$ nm. The rapid acceleration of the tip in response to this much larger force causes a rotation about its center of mass that in this case is so rapid that the position of the clamp x_0 actually moves in the opposite direction *in the laboratory frame*, which causes the apparent increase in separation and a positive increment to the apparent deflection. At the highest driving velocity,

where prior to h^* the total negative apparent deflection is small, the increment is sufficient to make the apparent deflection $\tilde{x}_1(x_0)$ positive. By the conventional static interpretation, this positive deflection would be interpreted as a repulsive force. In fact of course it is a consequence of the extremely strong van der Waals attraction approaching contact, and of the dynamics of the force measuring procedure.

As mentioned above the base of the kink corresponds to the surface jump into contact. The top of the kink corresponds to the next change in direction of the motion of the actual bodies, which occurs at the deepest penetration [$h=-6.32$ nm in Fig. 5(a)]. This change in direction of x_1 is levered by the length of the tip and produces the change in motion of x_0 , which is the transient that induces the vibrations in the cantilever beam. The amplitudes of these vibrations are much larger in Fig. 5 than in Fig. 4, due essentially to the greater amount of energy being available in the deformed case. The van der Waals potential energy that is converted into kinetic energy by the collision is essentially the surface energy times the contact area; the latter is much larger for the mutually flattened deformed bodies than it is if deformation is not allowed. The amplitude of the apparent oscillations (half the difference between successive extrema in the apparent separation) is 9.4 nm at the fastest driving velocity [$6.4 \mu\text{m s}^{-1}$, Fig. 5(a)], and 8.8–8.7 nm for all the other speeds examined (3.2 – $0.16 \mu\text{m s}^{-1}$). This may be compared to the amplitude in the absence of deformation, Figs. 4, namely 4.7–3.2 nm. Hence not only is the amplitude of the apparent oscillations larger, but they also are less dependent on the driving velocity when deformation is taken into account. The frequency of the vibrations is of course still close to the calculated resonance of the beam in contact, namely 331 Hz.

Turning now to the actual undeformed separation, what is noticeable in Fig. 5 compared to Fig. 4 is the negative values. In particular, for high loads (large positive deflections) the actual undeformed separation is close to -3.3 nm. This represents flattening of the surfaces from their unstressed spherical shape; the amount of deformation is $\delta=h-H_0=-3.3-0.3=-3.6$ nm. Except for immediately following the surface jump into contact, the flattening hardly changes at all over the range of loads in the figures. [Figures 5(b) and 5(c) show only tensions, but we have performed the calculations up to positive loads corresponding to deflections on the order of 10^2 nm, with little change. We shall show below that the effective spring constant for elastic deformation under positive load is on the order of 10^5 N m $^{-1}$.] Hence the primary effect of deformation is a shift in the zero of the undeformed actual separation compared to the physical separation.

After the surfaces of the bodies have jumped into contact, the position of the center of mass of the bodies (which corresponds to h and x_1) oscillates about the eventual flattened position $h=-3.3$ nm. (Just after initial contact the center line of the oscillations is at more positive deformations and shows noticeable curvature.) These oscillations are the analogue of the bouncing of the rigid bodies of Fig. 4, and as in that case they are a consequence of conservation of energy in the collision. Since the physical surface separation

is fixed at H_0 , the post-contact oscillations represent elastic vibrations of the bodies. The deformation changes alternately from flattened to extended as the centers of mass approach and recede from each other with their surfaces fixed in contact.

The frequency of the elastic vibrations may be calculated using an effective spring constant. This arises from the elasticity of the bodies and is defined by

$$k_e = \frac{dF_\delta}{d\delta} = \left(\frac{da}{dF_\delta} \frac{d\delta}{da} \right)^{-1}. \quad (33)$$

This equation for the effective spring constant of compliant bodies is of a general character, that can be used to correct static surface force measurements for the post-contact situation. In the precontact situation Parker and Attard^{28,30} have mapped the undeformed surface separation to the physical surface separation by using the measured force and an effective spring constant for the elastic bodies.

The JKR expression may be used to evaluate this equation. For moderate compressions one can expand about the result for zero load. Using the contact area under zero load,

$$a_0 = [9\pi\gamma R^2(1-\nu^2)/4E]^{1/3}, \quad (34)$$

one has

$$\frac{d\delta}{da} = \frac{4a_0}{R} - \sqrt{\frac{\pi\gamma(1-\nu^2)}{a_0E}}, \quad (35)$$

and

$$\frac{da}{dF_\delta} = \frac{R(1-\nu^2)}{2Ea_0^2}. \quad (36)$$

For the present parameters [$E/(1-\nu^2) = 6 \times 10^{10} \text{ N m}^{-2}$, $R = 1.45 \text{ mm}$, $\gamma = 0.8 \text{ J m}^{-2}$] this gives $k_e = 10^5 \text{ N m}^{-1}$. (This is relatively constant with increasing load, but is about 30% smaller at the maximum tension.) This is much higher than the force-measuring spring constant, $k = 89 \text{ N m}^{-1}$ (which justifies the above statement that the primary static effect of elastic deformation is to shift the zero of separation), and we need not consider the latter further. In fact we can imagine that the base of the tip x_0 is fixed (because the frequency of these elastic vibrations is so much higher than the resonant frequency of the cantilever) and so the effective mass for the elastic vibrations is essentially the moment of inertia of the tip rotating about its base $m_1/3$. This gives for the frequency of the elastic vibrations $f = (1/2\pi)\sqrt{3k_e/m_1} = 2.7 \text{ kHz}$. The numerical calculations in Fig. 5 give 2.8 kHz, which confirms their accuracy and validity.

III. EXPERIMENT

Measurements were made of the van der Waals force between glass surfaces in air, using the MASIF, which has previously been described in detail.¹ The surfaces were made by melting the ends of Pyrex rods to form spherical caps. The caps are of uniform curvature and molecularly smooth,¹ and their average radius was measured to be 1.045 mm. The force measuring spring constant was 87.2 N m^{-1} , which was determined gravitationally as described above. The position

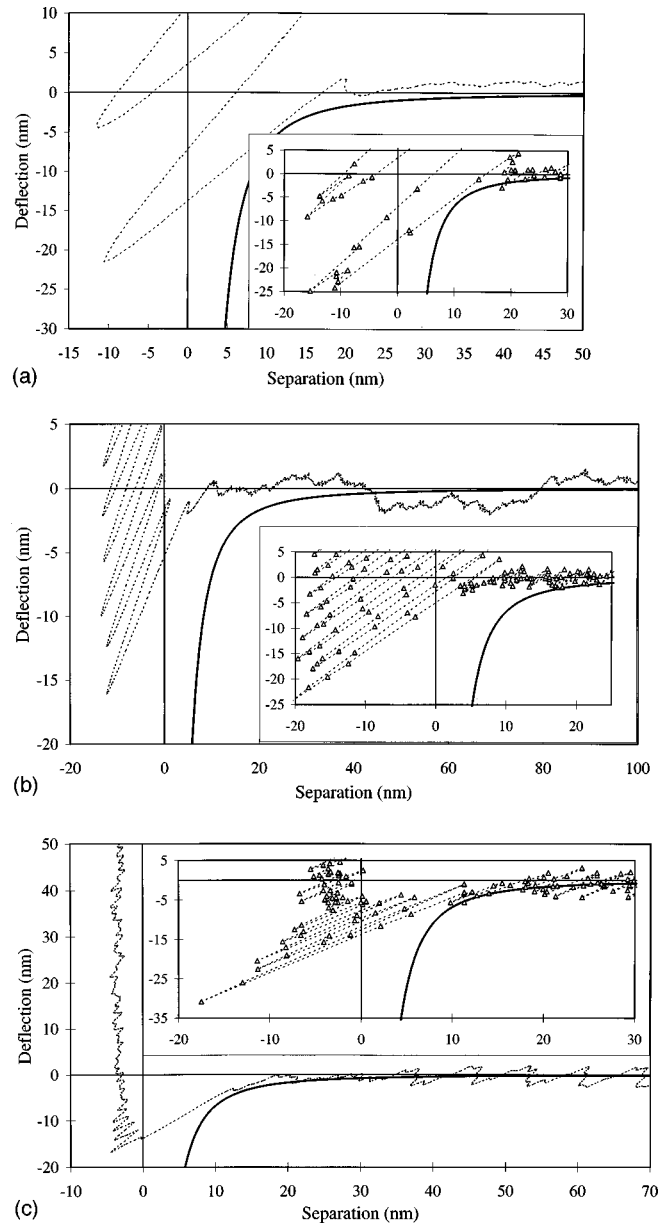


FIG. 6. Dynamic force measurement using the MASIF of the van der Waals interaction between glass surfaces in air. In the main figure the experimental data (dotted curve) have been smoothed with a seven point moving average. The apparent deflection is inferred from the bimorph voltage, as calibrated in the constant compliance regime under steady driving conditions. The zero of the undeformed apparent separation has been set equal to -3.5 nm , as calculated using JKR theory. The bold curve is the static deflection due to the van der Waals attraction ($A = 5 \times 10^{-19} \text{ J}$, $R = 1.45 \text{ mm}$, $k = 87.2 \text{ N m}^{-1}$). The inset shows the jump into contact on an expanded scale; the symbols are actual data, measured at equal time intervals (different in each figure). (a) The driving velocity is $\dot{z} = 6.11 \mu\text{m s}^{-1}$, and a datum is measured every 0.1 ms , (b) $1.57 \mu\text{m s}^{-1}$, and 0.2 ms , (c) $0.16 \mu\text{m s}^{-1}$, and 2 ms .

of the piezo-mounted driving surface was measured with a linearly variable distance transducer, using a polynomial fit, as described previously.¹ The bimorph response was calibrated in the constant compliance regime as usual. No attempt was made to control the humidity in the experiments reported below.

Figure 6 shows dynamic force measurements of the van der Waals attraction using the MASIF. In all we measured

forces at six different driving speeds, with 4–8 repeat experiments in each case. The present selection spans the dynamic range that we measured, and the data are typical of the results that we obtained. All of the features found in the theoretical modeling occurred consistently in the dynamic force measurements. Features that can be seen in the figures include the lack of a measurable attraction approaching contact and the noticeable kink at about $\tilde{h} = 15$ nm, particularly at the highest driving velocities, and, in addition, the extremely rapid apparent jump into contact and the large amplitude postcontact oscillations.

At high speeds of approach, Fig. 6(a), there is no evidence of the van der Waals attraction at large separations. This is consistent with Figs. 4(a) and 5(b), which predict a deflection of about 1 nm prior to the kink. The noise level of the device due to mechanical vibrations is in these particular experiments of similar magnitude, which makes it difficult to discern unambiguously such a weak precontact attraction. Here the noise induces two resonant vibrations: one at 66 Hz and the other at 24 Hz. (There is also electrical noise of much higher frequency.) The higher resonance is just the fundamental resonant frequency of the cantilever, and at this velocity it corresponds to 48 nm per period. The low frequency resonance appears to be one of the modes of the whole apparatus bouncing on its elastic cords. The data lying above the abscissa between 20 and 50 nm in Fig. 6(a) result from the combination of the two motions. It is not possible to shield completely the device from mechanical or acoustic noise. Due to the low viscosity of air these resonances do not decay as rapidly as they do in liquids, which limits the accuracy that can be achieved in these particular measurements.

The apparatus resonance is more evident in Fig. 6(b), (65 nm per period) with the cantilever resonance (24 nm per period) superimposed. In Fig. 6(c) the apparatus resonance is very well defined (6.6 nm per period), whereas the fundamental resonance of the cantilever has been suppressed in the figures by the seven-point moving average that was used to smooth the data. (In this case the seven points span 12 ms, which is almost the period of the resonant vibrations, 15 ms.) The data taken at the slowest driving speed [Fig. 6(c)] clearly shows the van der Waals interaction between the two surfaces at long range. Between 20 and 35 nm there is a noticeable decrease in the amplitude of the mechanical vibration of the cantilever as the van der Waals interaction couples the two surfaces. The results are consistent with Fig. 5(c), where it can be seen that the surfaces do indeed interact at this range at this slow speed of approach. The van der Waals attraction prior to contact is also manifest in Fig. 6(c) by the close agreement of the measured data with the calculated static van der Waals deflection down to 10 nm. According to Fig. 5(c), at about this point the effects of inertia become evident and one begins to see a discrepancy between the static and dynamic deflections. The inset of Fig. 6(c) graphically shows the measured jump into contact; in this regime the apparent deflection is close to the actual deflection [Fig. 5(c)]. [Note that the seven-point smoothing in the main part of Fig. 6(c) is a little misleading around contact because the

low sampling rate means that the few data points ill define the rapid variations].

The apparent jump into contact is preceded by a kink that is most evident at the highest driving speed. Close inspection of the inset of Fig. 6(a) shows that the kink is very well defined and significantly above the noise levels of the device. The height of the kink is about 5 nm, compared to 2 nm calculated in Fig. 5(a). (The discrepancy between the calculated and measured apparent amplitudes is discussed below.) This kink that signifies the instant of actual contact was present in all the experiments that we performed at high driving velocities.

The physical elastic bounces are not directly measured in Fig. 6(a) (in the sense that it is the apparent, not the actual, deflection that is measured). Nevertheless, just as they appear in Fig. 5(a), the effects of several of the elastic bounces are visible, superimposed on the first vibration of the cantilever. The time of the first elastic bounce, from the top of the kink to the paired points half way down the apparent jump into contact, is five data points or 0.4 ms, giving a frequency of 2.5 kHz. (The time between successive data samples is 0.1 ms in this case.) Alternatively, one can make out the first three bounces at $(\tilde{h}, \tilde{x}_1) = (0, -15)$, $(-20, -25)$, and $(-10$ nm, -15 nm), which correspond to the three apparent bounces in Fig. 5(a) at $(\tilde{h}, \tilde{x}_1) = (-3, -5)$, $(-9, -9)$, and $(-12$ nm, -8 nm), respectively. The 12 data points that define these three bounces give a frequency of $3/(11 \times 0.1) = 2.7$ kHz, which is in embarrassingly good agreement with the 2.8 kHz of Fig. 5, and the 2.7 kHz calculated from the effective elastic spring constant for the bodies, Eqs. (33)–(36).

We measure the frequency of the post-contact vibrations of Fig. 6 and our other data to be about 350 Hz. [The 2 ms sampling of Fig 6(c) is too coarse to give the post-contact oscillations reliably.] This is in good agreement with the fundamental vibration of the cantilever beam with the tip fixed in contact, calculated to be 331 Hz, [Eq. (25), Figs. 4 and 5]. This confirms the validity of our model of dynamic force measurement, including the distinction that we make between the actual and the apparent deflections. The fact that the measurements really give the latter quantity is shown by the harmony between the frequency of cantilever resonant vibrations and the measured post-contact oscillations.

One can identify at least two further similarities between the calculations and the measurements. These concern the qualitative dependence of the amplitude of the post-contact oscillations on the driving velocity. First, in going from the fastest to the slowest driving velocity ($\dot{z} = 6.4, 0.16 \mu\text{m s}^{-1}$), the calculated amplitude decreases, (9.4, 8.7 nm), as does the measured one (20, 15 nm). This decrease is due to the lower kinetic energy of the collision. Second, the apparent separation at which the kink occurs is less than the maximum post-contact apparent separation (which occurs at the end of the first vibration) in both the theoretical calculations (Fig. 5) and in the measured data (Fig. 6). In both cases the discrepancy between the two decreases with decreasing driving velocity; in the slowest case [Figs. 5(c) and 6(c)] the two are approximately equal.

The amplitudes of the calculated and measured post-contact vibrations are not in quantitative agreement. In Fig 5(a) it is 9.4 nm, whereas in Fig 6(a) it is 20 nm. [Note that the running average used to smooth the experimental data in the main figures diminishes the amplitude of the post-contact vibrations; the value of 20 nm comes from the inset of Fig. 6(a), and repeat measurements not reproduced here]. The main reason for the discrepancy appears to be the oversimplification in the calculation of the apparent deflection, $\tilde{x}_1(x_0)$, namely that the bimorph response was taken to be solely proportional to the deflection of its end x_0 . In reality the voltage produced by the bimorph will be a functional of its shape, which includes, but is not restricted to, the deflection of its end. A second contribution to the discrepancy between the magnitude of the calculated and measured amplitudes is the use of the JKR approximation to estimate the adhesion and deformation of the bodies. As shown by Attard and Parker,²⁷ this approximation has restricted accuracy in the regime of these particular experiments, ($\sigma=5$).

Another difference between the calculations and the measurements is the decay of the vibrations. The measured amplitudes decay relatively quickly; at the highest driving velocity the amplitude has decreased by 25% after four vibrations. In contrast the calculated amplitudes do not decay noticeably at all. We carried out some calculations invoking Stokes drag for the motion of the cantilever (in addition to the drainage dissipation due to the motion of the surfaces) but the effect was almost negligible. It appears that the reason for the difference is that in the model the coupling between the cantilever and the motion of the surfaces only includes the motion of x_1 . One should also include the contribution due to changing the angle θ , since the cantilever vibrations represent variations in the angle at constant deflection. In other words, the elastic force that we take from JKR theory is for a normal load, so that it is derived from an elastic potential that depends only upon the central deformation which in turn depends only upon the deflection $U_\delta(x_1)$. In reality the change in angle of the tip as the cantilever vibrates represents the application of an additional torque, and one should really deal with $U_\delta(x_1, \theta)$, in which case the contact region is no longer circular. Including this increased, more realistic coupling of the cantilever motion to the surface motion and deformation in the model calculations would dissipate the energy of the cantilever vibrations more efficiently, causing their amplitude to decay as is observed in the experiments.

A final phenomenon that was not included in the theoretical calculations is the possibility of capillary condensation, which could occur because the experiments were performed without controlling the humidity. It is possible that a molecularly thin wetting layer of water has condensed on each surface and that their interaction contributes to the measurements. It is also possible that a water bridge could condense during the force measuring process itself, drawing the surfaces into contact, depending upon the rates of diffusion in the region between the two surfaces. We have no direct evidence for either of these possibilities, but neither can we rule them out. It is known that capillary condensation occurs around the perimeter of the contact zone after the surfaces

have come into contact. This will primarily affect the adhesion and the pull-off force, which are not our main concern here.

Although the theory underestimates the amplitude, the calculations qualitatively account for the behavior of the post-contact apparent oscillations in the experiments. The theory may be described as quantitative in its description of the various frequencies: the predicted and measured elastic vibrations are in harmony, and the calculated and actual cantilever frequencies are consonant. The broad agreement between the theory and the experiments validates the present model of the dynamic force measuring process. The calculations offer a clear physical interpretation of the various features of the measured data, demonstrating that the lack of precontact attraction is an inertial effect, and quantifying the conceptual distinction between the apparent and the actual deflection and separation.

IV. DISCUSSION

Dynamic surface force measurements potentially suffer from a number of artifacts, but they also offer certain opportunities not available to conventional static measurements. On the negative side, inertia causes the deflection of the cantilever or force measuring spring to be less than it would be for a static or equilibrium measurement. Hence simply equating the measured deflection to the surface force (i.e., Hooke's law) will underestimate the magnitude of the latter in those cases where inertia is significant. As shown in the text, Eq. (7), it is not permissible to use Hooke's law for massive bodies and weak springs (low resonant frequencies) or for fast driving velocities, or in regions of rapidly changing forces, or when high precision is required.

Related to inertia, and similarly problematic, is the dynamic decoupling of deflection and angle of the force measuring cantilever. In the static or steady state situation variations in each are linearly proportional, and hence one can be deduced from the other. This is not the case when acceleration occurs, and the consequence of measuring only the angle, for example, is the inability to deduce the deflection. In other words, one cannot apply the calibration factor deduced in the steady state constant compliance region to the transient, dynamic regime. Dynamic decoupling causes uncertainty about the separation and the force between the surfaces.

These two problems (inertia and dynamic decoupling) can be overcome by solving the equations of motion of the system. This allows the surface force to be measured by fitting the calculated trajectory to the measured one. Although obviously less convenient than a static force measurement, where one simply equates the surface force to the measured deflection via Hooke's law, it does provide a workable solution in those situations where inertial effects cannot be avoided. This approach was taken here for the van der Waals force, which was measured between glass surfaces in air. We found that a value of the Hamaker constant of 5×10^{-19} J was able to describe our data for a range of driving velocities.

One of the benefits of dynamic surface force measure-

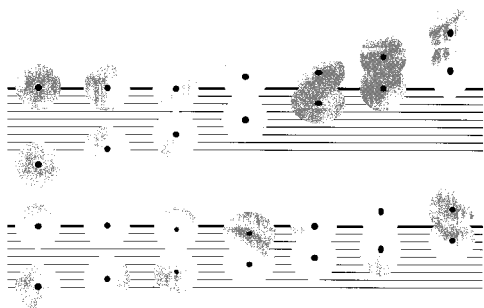


FIG. 7. Two adhesive elastic spheres colliding. The snapshots represent equal time slices, with the lower sphere moving at constant velocity. The initially stationary upper sphere is mounted on a spring: deflection below the bold line corresponds to an attraction, and deflection above to a repulsion. In the lower sequence the collision occurs sufficiently slowly that the van der Waals attraction is measurable. In the upper sequence the lower sphere is moving twice as fast and the upper sphere does not have time to respond to the attraction. The collision induces elastic vibrations in the spheres, which is manifest as an oscillatory deflection of the spring superimposed upon the linearly increasing repulsion (constant compliance).

ment is the new area of research that it opens up. What one is now able to do is to monitor the dynamics of a collision between moving bodies at the molecular level. Hence the results obtained in the present paper are in fact a measurement of an elastic collision between two adhesive spheres. With a high sampling rate we were able to see the deformation and mutual wetting of the surfaces, and the elastic vibrations induced by the collision. The collision process is depicted in Fig. 7. Movement of the upper body prior to contact, evident for a slow collision, does not occur for a fast collision due to inertia. In both cases however the bodies mutually adhere after the collision, and the contact region becomes flattened. The collision induces elastic vibrations in the bodies, the amplitude of which depends upon the violence of the collision.

The frequency of these vibrations depends upon the elasticity of the bodies. Hence it would be possible to use the data as a direct measurement of Young's modulus. We have performed such measurements for polymer spheres, which show low frequency, large amplitude vibrations due to their high flexibility. We shall report the results in due course. In

the second article in this series,¹⁵ where we deal with the atomic force microscope, we address the role of friction in dynamic surface force measurement.

- ¹J. L. Parker, *Prog. Surf. Sci.* **47**, 205 (1994).
- ²J. L. Parker, *Langmuir* **8**, 551 (1992).
- ³G. Binnig, C. F. Quate, and C. Gerber, *Phys. Rev. Lett.* **56**, 930 (1986).
- ⁴W. A. Ducker, T. J. Senden, and R. M. Pashley, *Nature (London)* **353**, 239 (1991).
- ⁵P. M. Claesson, T. Ederth, V. Bergeron, and M. W. Rutland, *Adv. Colloid Interface Sci.* **67**, 119 (1996).
- ⁶M. J. Spaarnay and P. W. J. Jochems, *Proceedings of the 3rd International Conference Surface Activity*, Vol. 2, p. 375.
- ⁷D. Tabor and R. H. S. Winterton, *Proc. R. Soc. London, Ser. A* **312**, 435 (1969).
- ⁸J. N. Israelachvili and D. Tabor, *Proc. R. Soc. London, Ser. A* **331**, 19 (1972).
- ⁹K. B. Lodge and R. Mason, *Proc. R. Soc. London, Ser. A* **383**, 279 (1982); *ibid.* **383**, 295 (1982).
- ¹⁰Y. Martin, C. C. Williams, and H. K. Wickramasinghe, *J. Appl. Phys.* **61**, 4723 (1987).
- ¹¹T. R. Albrecht, P. Grütter, D. Horne, and D. Ruger, *J. Appl. Phys.* **69**, 668 (1991).
- ¹²Q. Zhong, D. Inniss, and V. B. Elings, *Surf. Sci.* **290**, L688 (1993).
- ¹³A. M. Stewart and J. L. Parker, *Rev. Sci. Instrum.* **63**, 5626 (1992).
- ¹⁴D. Y. C. Chan and R. G. Horn, *J. Chem. Phys.* **83**, 5311 (1985).
- ¹⁵P. Attard, A. Carambassis, and M. W. Rutland (unpublished).
- ¹⁶P. Gleyzes, P. K. Kuo, and A. C. Boccardo, *Appl. Phys. Lett.* **58**, 2989 (1991).
- ¹⁷J. P. Spatz, S. Sheiko, M. Möller, R. G. Winkler, P. Reineker, and O. Marti, *Nanotechnology* **6**, 40 (1995).
- ¹⁸B. Ancykowski, D. Krüger, and H. Fuchs, *Phys. Rev. B* **53**, 15485 (1996).
- ¹⁹P. Fontaine, P. Guenoun, and J. Daillant, *Rev. Sci. Instrum.* **68**, 4145 (1997).
- ²⁰M. Tsukada, N. Sasaki, R. Yamura, N. Sato, and K. Abe, *Surf. Sci.* **401**, 355 (1998).
- ²¹R. J. Warmack, X.-Y. Zheng, T. Thundat, and D. P. Allison, *Rev. Sci. Instrum.* **65**, 394 (1994).
- ²²J. M. Neumeister and W. A. Ducker, *Rev. Sci. Instrum.* **65**, 2527 (1994).
- ²³R. V. Southwell, *An Introduction to the Theory of Elasticity* (Oxford, London, 1936).
- ²⁴J. P. Cleveland, S. Manne, B. Docek, and P. K. Hansma, *Rev. Sci. Instrum.* **64**, 403 (1993).
- ²⁵G. Y. Chen, R. J. Warmack, T. Thundat, and D. P. Allison, *Rev. Sci. Instrum.* **65**, 2532 (1994).
- ²⁶K. L. Johnson, K. Kendall, and A. D. Roberts, *Proc. R. Soc. London, Ser. A* **324**, 301 (1971).
- ²⁷P. Attard and J. L. Parker, *Phys. Rev. A* **46**, 7959 (1992); *Phys. Rev. E* **50**, 5145 (1994).
- ²⁸J. L. Parker and P. Attard, *J. Phys. Chem.* **96**, 10398 (1992).
- ²⁹H. Tang, C. Joachim, and J. Devillers, *Europhys. Lett.* **30**, 289 (1995).
- ³⁰P. Attard and J. L. Parker, *J. Phys. Chem.* **96**, 5086 (1992).